Journal of Applied Fluid Mechanics, Vol. 18, No. 3, pp. 742-755, 2025.
Available online at www.jafmonline.net, ISSN 1735-3572, EISSN 1735-3645.
https://doi.org/10.47176/jafm.18.3.2866

Propeller Slipstream Effects on the Aerodynamics Characteristics of a Transition Micro Air Vehicle

A. Vinoth Raj †and C. Senthil Kumar

Department of Aerospace Engineering, Madras Institute of Technology, Anna University, Chrompet, Chennai-600 044, Tamil Nadu, India

†*Corresponding Author Email: vinothraj@mitindia.edu*

ABSTRACT

This study investigates the influence of propeller slipstream on the aerodynamic characteristics of a Transition Micro Air Vehicle (TMAV). The TMAV under consideration comprises a cylindrical body, planar wing, and X-tails. Wind tunnel testing and numerical simulations were performed on TMAV configurations both with and without a propeller at various advance ratios (J = 0.45, 0.55, 0.65, and 0.75). The angle of attack ranged from -8° to +8° in increments of 4°, and from +8° to +16° in increments of 1°. The findings indicate that propeller slipstream significantly alters the flow field around the TMAV components, leading to a reduction in overall aerodynamic performance and stability. Specifically, the slipstream downwash decreased the lift and drag of the port wing and certain tails, while the slipstream upwash increased the lift and drag of the starboard wing and other tails, resulting in earlier stall occurrences under slipstream conditions. Furthermore, it was observed that aerodynamic performance improves as the propeller advance ratio decreases. The data obtained from this study elucidate the effects of propeller slipstream on the aerodynamic performance of wing and X-tail combined MAVs. Currently, there is a lack of literature addressing the effects of propeller slipstream on the aerodynamics of wing and X-tail combined MAV configurations. This study provides valuable insights into the aerodynamic behavior of this TMAV under the influence of propeller slipstream.

Article History

Received May 22, 2024
Revised July 11, 2024
Accepted October 1, 2024
Available online January 1, 2025

Keywords:

Interactional aerodynamics
Wings downwash
X-tail deflection effects
Multiple Reference Frame (MRF) technique
MAV stability

1. INTRODUCTION

Micro air vehicles (MAVs) are rapidly becoming essential in various operations, such as reconnaissance, rescue, and surveillance, and are also increasingly significant in tactical settings (Hassanalian et al., 2015). The vehicles falling within the category of MAVs are characterized by a maximum size of less than 10cm, a mass of around 90g, or an endurance of less than one hour (Sadraey, 2010). Fixed-wing MAVs are superior due to their silence, endurance, payload capacity, speed, altitude, and lack of audibility. A tractor propeller configuration is usually used for most fixed wing MAVs. Due to the tractor-type MAV configuration, the distributed propeller slipstream flow interacts extensively with a significant portion of the MAV's control surfaces. The propeller slipstream presents a complex flow characterized by high swirl velocity and an increasing axial flow component in the streamwise direction. This complexity poses challenges for accurately predicting the aerodynamic interference between the propeller and MAV surfaces in research endeavors. This interaction has an intensive impact on the MAV stability and aerodynamic characteristics. Therefore, it is imperative to thoroughly understand the comprehensive aerodynamic characteristics and flow patterns on MAV surfaces influenced by the propeller slipstream flow. This understanding is important for the optimal design of a fixed-wing MAV powered by a propeller. The propeller MAV surfaces aerodynamic interaction has been thoroughly investigated using both CFD studies and experimental techniques (Catalano, 2004; Teixeira & Cesnik, 2019; Rostami & Farajollahi, 2021; Zhao et al., 2022).

The flow generated by propellers typically alters the drag polar, lift curve slope, and affects flow transition and separation. MAVs are typically operated at low Reynolds numbers and have a low aspect ratio, usually less than 2. In this regime, there is a significant reduction in the lift-to-drag ratio due to the formation of laminar separation bubbles (Jana et al., 2020). For propeller-driven MAVs,

NOMENCLATURE

AF	Axial Force
C_D	drag coefficient
C_{D0}	zero lift drag coefficient
C_L	lift coefficient
C_M	pitching moment coefficient
d	propeller diameter
F	thrust
L/D	lift to drag ratio
J	propeller advance ratio
N1	normal force at location 1 in internal balance
N2	normal force at location 2 in internal balance
T1	location at tail 4 in unpowered cases
T2	location at tail 3 in un powered cases
T1(P)	location at tail 4 in powered cases
T2(P)	location at tail 3 in powered cases
W1	location at near wing root in unpowered cases
W2	location at near wing tip in unpowered cases
W1(P)	location at near wing root in powered cases
W2(P)	location at near wing tip in powered cases
Y^+	non-dimensional wall distance
α	angle of attack (AoA)
k	turbulence kinetic energy
ω	specific dissipation rate
Definitions	
CFD	Computational Fluid Dynamics
CG	Center Of Gravity
FRP	Fiber-Reinforced Plastic
MRF	Multiple Reference Frame
MAV	Micro Air Vehicle
RPS	Revolution Per Second
SST	Shear Stress Transport
VTOL	Vertical Take-Off And Landing
UAV	Unmanned Air Vehicle

the size of the propeller is comparable to the wing dimensions, resulting in a significant impact of the propeller-induced flow on overall aerodynamics, including the formation of laminar separation bubbles (Chinwicharnam & Thipyopas, 2016), flow transition (Aminaei et al., 2019), and flow separation. The propulsive forces were impacting important factors including the stall AoA (Arivoli et al., 2011), lift and drag coefficients (Durai, 2014), L/D ratio (Ananda et al., 2013), and pitching moment (Ahn & Lee, 2013), among others. Propeller flow has a significant impact on the transition from laminar to turbulent flow (Ananda et al., 2018). The aerodynamic impact of propeller slipstream on both wing-alone and MAV configurations is evaluated using numerical simulations (Chen & Yang, 2022; Wang & Zhou, 2022; Cao et al., 2023; Meng et al., 2023; Furusawa et al., 2024) and wind tunnel experiments (Null & Shkarayev, 2005; Arivoli et al., 2011; Ananda et al., 2013; Sudhakar et al., 2013; Chinwicharnam & Thipyopas, 2016; Sharma & Atkins, 2019).

The wind tunnel experiment conducted on a MAV with a 30cm wingspan and an inverse Zimmerman planform revealed that within a Reynolds number range of 120,000 to 180,000, the propeller-induced flow enhances the lift coefficient and delays stall (Arivoli et al., 2011). Similarly, experiments were conducted on an inverse Zimmerman platform MAV with propeller speeds ranging from 8000 to 10000 RPM. The results indicated an increase in the lift coefficient at higher angles of attack (AoA) and an increase in the drag coefficient due to the propulsive slipstream flow (Durai, 2014). A study by (Furusawa et al., 2024) investigated the interaction between propeller and wing using the overset grid numerical method. Their findings indicated that as the propeller advance ratio increased, the wing lift coefficient also increased. The study employed three different advance ratios: 0.8, 0.6, and 0.4. For an advance ratio of J=0.8, the wing lift coefficient was lower than in the unpowered scenario. At J=0.6, the wing lift coefficient was comparable to the unpowered case. Notably, at J=0.4, the wing lift coefficient exceeded that of the unpowered condition. In research, (Meng et al., 2023) examined propeller slipstream flows in a channel wing configuration using the MRF method for simulations. Their findings showed that employing a tractor propeller increased the channel wing lift coefficient and decreased drag coefficients. The experiments by (Zhang et al., 2023) were conducted on an electric propulsion aircraft equipped with a high-lift ducted fan in subsonic wind tunnels. The tests were performed at various free stream velocities (15 to 25 m/s), AOAs (-4˚ to 16˚), and deflection angles. The results indicated that the use of a series of propellers led to enhanced lift and reduced drag. Shams et al. (2020) conducted experiments in a subsonic wind tunnel on a MAV to investigate the effects of propeller slipstream. The study involved testing at three different free stream velocities, three propeller rotation speeds, and with three different propellers.

The results indicated that increasing the propeller rotational speed led to higher aerodynamic coefficients, although it resulted in a reduction in the lift-to-drag ratio. Additionally, the pitching moment coefficients showed a linear variation with a negative gradient, whereas the rolling and yawing moment coefficients exhibited non-linear behavior. The CFD study by (Rostami & Farajollahi, 2021) utilized a UAV with twin propellers and a duct, employing the MRF method. The findings indicated that the rear engine propeller increased UAV efficiency by 10%, while the ducted propeller configuration exhibited 6% higher efficiency compared to the non-ducted propeller configuration. In numerical analysis, (Figat & Piątkowska, 2020) investigated a combined configuration featuring a pusher propeller and fuselage. The findings indicated that the pusher configuration demonstrates superior efficiency compared to the tractor configuration. Cao et al. (2023) conducted a numerical investigation to assess the influence of propeller slipstream on UAV wings using the actuator disk method. The study revealed that increasing the propeller size led to corresponding increases in wing lift coefficients. Additionally, showed that co-rotating propellers achieved higher lift coefficients compared to counter-rotating propellers. This study proposed configuration

demonstrated a significant improvement, increasing the lift-to-drag (L/D) ratio by 7.34%.

In wind tunnel experiments, flat plates with aspect ratios of 2, 3, and 4 were tested with varying propeller speeds. Both tractor and pusher configurations showed increased stall delay and lift coefficients (>40%) with higher propeller speeds. However, as aspect ratio increased, flat plate performance decreased (Ananda et al., 2014). In study (Jana et al., 2020), experimental investigations on a biplane MAV (chord: 140mm, span: 150mm) revealed that propeller slipstream flow enhances lift and drag forces, pitching and rolling moments, range, and endurance, with minimal impact on yawing moment. In (Chinwicharnam & Thipyopas, 2016), experiments on pusher and tractor-type tilt body MAVs were conducted at free stream velocities of 6 and 10 m/s, and propeller advance ratios from 0.225 to 0.5. These results showed that the pusher-type MAV had lower maximum lift coefficient, stall angle, and aerodynamic efficiency compared to the tractor-type MAV, which exhibited a higher lift-to-drag ratio. In contrast, numerical simulations were conducted for a High-Altitude Long Endurance (HALE) UAV using the MRF method to model propeller rotation. This MAV comprises a body, wing, and V-tail. The results showed a decrease in lift coefficient by 0.07% and an increase in drag coefficient by 3.53% (Chen et al., 2015) and another CFD analysis for a solar-powered UAV in a flying wing configuration explored angles of attack (AoAs) from 0 to 20 degrees (Wang & Zhou, 2022). These results showed decreased lift coefficients and lift-to-drag ratios, increased drag coefficients, and improved pitching stability at high AoAs.

The wind tunnel test and unsteady CFD analysis of a propeller-driven UAV (Cho, 2014) found that power-on effects mainly increase slipstream drag and nose-up pitching moment, with negligible impact on lift coefficients. Ananda et al. (2014) results show an increment in L/D ratio due to propeller slipstream, and another wind tunnel experiment (Khoshnevis et al., 2016) demonstrated that higher angles of attack (AoA) lead to a higher lift-to-drag (L/D) ratio, while lower AoA results in a lower L/D ratio due to propeller slipstream. Additionally, numerical results from (Chinwicharnam & Thipyopas, 2016) shows that the L/D ratio is higher for the tractor configuration compared to the pusher configuration. Furthermore, (Ahn & Lee, 2013) reported an increase in the slope of the pitching moment curve and pitching moment due to propeller slipstream. Previous research on the effects of propeller slipstream on the aerodynamics of aircraft, UAVs, and MAVs has examined various configurations, ranging from wing-alone designs to those incorporating conventional tails. These studies report mixed outcomes, with some indicating increases in aerodynamic parameters and others noting decreases. Consequently, these parameters vary with flight vehicle configurations. To the author's knowledge, there is no mention in the extant literature of the effect of propeller slipstream on the aerodynamic characteristics of a wing and X-tail combined micro air vehicle. This study investigates the impact of propeller-induced flow on the aerodynamic parameters and stability of a Transition Micro-Air Vehicle (TMAV).

This TMAV, with a body length of 1m and a mass of 1.3 kg, falls within the small UAV category, with a range of 0.5km and endurance of less than 1 hour, according to (Sadraey, 2010). Thus, it is classified as a MAV. This TMAV is designed for VTOL applications, with a mission profile including vertical take-off and landing, cruise, pull-up maneuver, and transition to horizontal flight. Thus, this TMAV has five different transition phases, earning it the name "transition micro air vehicle." Generally, VTOL MAVs are researched for angles of attack (AoA) ranging from 0 to 90 degrees, but this study only investigates low AoAs (-8˚ to 16˚) due to lack of experimental facility. A number of wind tunnel experiments and CFD simulations were conducted on the TMAV, both with and without the propeller effect, at varying propeller advance ratios in a tractor configuration. Results indicate that propeller slipstream flow decreased the aerodynamic performance and increased the pitching moments. The novelty of this paper lies in the following aspects:

- ❖Mathematical quantification of the influence of propeller slipstream flow on aerodynamic parameters, derived from numerical analysis and wind tunnel experiments.
- ❖Investigation of propeller-slipstream flow effects on a fixed-wing and X-tail combined TMAV.

2. TMAV MODEL PARAMETERS

The model investigated in this study is a Transition Micro-Air Vehicle (TMAV) equipped with a tractor-type propeller. The CAD model, model design parameters and experimental model in wind tunnel test section are depicted in Fig. 1, while the parameters of the TMAV and its propeller are detailed in Table 1.

The TMAV under consideration features a cylindrical body with a rectangular wing and X-tails, exhibiting the following specifications: a cylindrical body diameter of 75

Table 1 TMAV Specifications

Part Name	Parameter	Value
Body	Shape	Circular
	Length	1010 mm
	Diameter	75 mm
	Material	Acrylic
Wing	Shape	Rectangular
	Span	882 mm
	Chord	145.5 mm
	Aerofoil	NACA 0015
	Material	Carbon FRP
Tail	Span	475.5 mm
	Chord	85.5 mm
	Aerofoil	NACA 0015
	Material	Carbon FRP
Motor	Type	Brushless
	KV (rpm/V)	650
	Brand	Avionic N4250
Propeller	Dimensions	13-inch × 8-inch

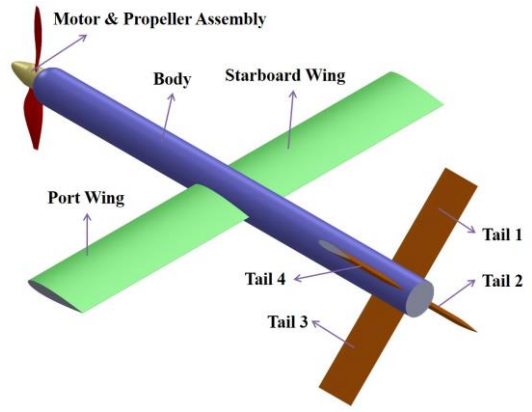

(a) CAD design model

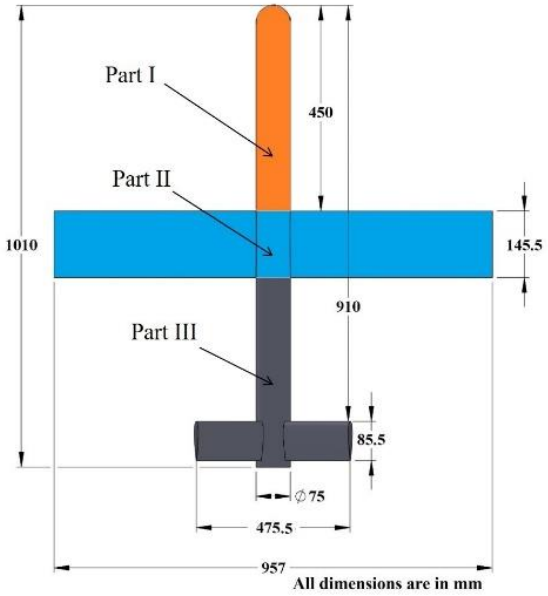

(b) Model design parameters

(c) Experimental model in wind tunnel test section

Fig. 1 TMAV Models

mm, a body length of 1010 mm, a wingspan of 882 mm, a wing chord of 145.5 mm, a planar tail span of 475.5 mm, and a tail chord of 85.5 mm. The NACA 0015 symmetrical airfoil is selected for both the wing and tail to prevent any misalignment during vertical takeoff and landing. The material density for the body is 1.6 g/cm³, while the surface density of the wing and tail material is 0.8 kg/m². The surface areas of the wing and tail are 0.2 m² and 0.08 m², respectively. The total mass of the vehicle is calculated to be 1.3 kg. The on-board equipment is arranged sequentially from the nose as follows: motor, battery, radio unit, actuators, and camera. The center of gravity (CG) location is influenced by the positions of the wing and control surfaces, which in turn depend on the CG. The vehicle's design parameters were established through an iterative design process aimed at achieving vertical takeoff and landing capability (Bansal et al., 2011), with the CG determined to be 0.519 m from the nose. The moment of inertia about the pitch axis is estimated to be 0.15 kg·m².

The experimental model is fabricated at a 1:1 scale ratio, consisting of three parts (Part I, Part II, and Part III) with a circular cross-section, made of 6 mm thick acrylic material, as illustrated in Fig. 1b. In Part I, provisions are made for the installation of the propulsion system, controller, and battery (for flight tests). In Parts II and III, the wings and control surfaces are attached separately to allow axial movement and are fixed rigidly to the body, with provisions for deflection. Carbon fiber reinforced plastic is chosen for the wings and control surfaces to minimize weight and enable reuse for flight test prototypes. The manufactured model's measurement precision is ±0.1%. A 2-blade constant-pitch propeller model, commonly used in MAV applications, is employed in this research.

3. Experimental and Computational Approach

3.1 Wind Tunnel Test

The wind tunnel test was conducted at the Aerodynamics Laboratory at the Madras Institute of Technology (MIT - Chennai) in India (Suresh et al., 2019) (Balaji et al, 2017). The test was performed in a subsonic, low-speed, and open-circuit wind tunnel with a closed test section.

The dimensions of the wind tunnel test section are 1.8 m in length, 1.2 m in width, and 0.9 m in height. The wind velocity range reached up to 45 m/s, and the turbulence intensity level was measured to be less than 1.5%. A pitot static tube was installed in the test section to measure the wind speed. A three-component internal balance was placed inside the experimental model. The experiments were conducted at a wind speed of 15 m/s, corresponding to a Reynolds number of 1.5×10^5 (based on wing chord). A constant free stream velocity of 15 m/s was maintained across all propeller advance ratios during the tunnel tests. The propeller was connected to a 650KV brushless motor mounted in the TMAV nose. An Arduino Uno board controlled the rotational speed of the propeller through the electronic speed controller during the tunnel tests. The overall experimental setup is shown in Fig. 2.

The propeller static thrust was calculated using theoretical equations, CFD simulations, and experiments.

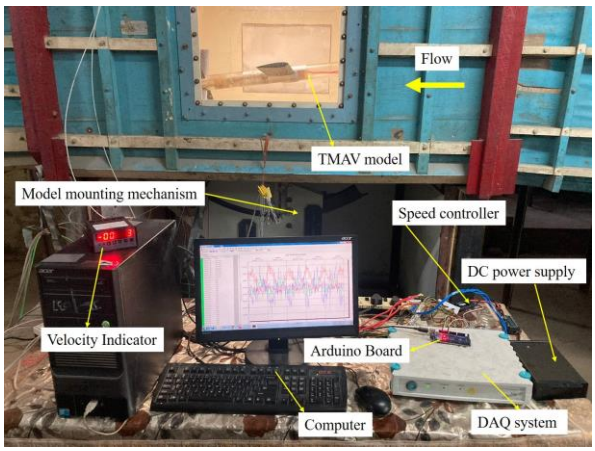

Fig. 2 Experimental setup

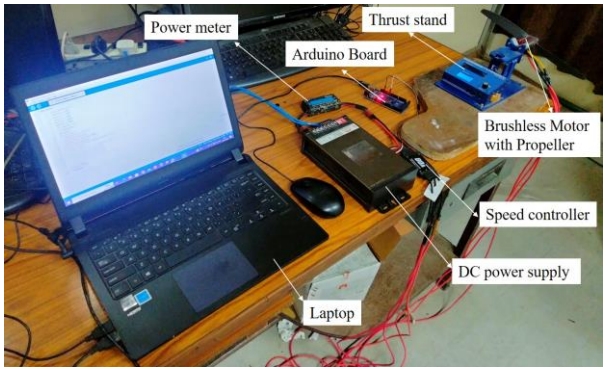

(a) experimental setup

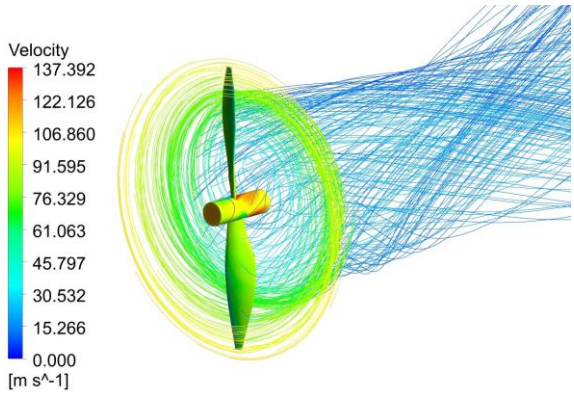

(b) CFD simulation

Fig. 3 Propeller static thrust testing

Eq. (1) (Gabriel, 2013) below was used to find thrust values:

$$F = 1.225 \left(\frac{\pi d^2}{4}\right)(RPS \times pitch)^2 \left(\frac{d}{pitch}\right)^{1.5} \quad (1)$$

The Turnigy thrust stand was utilized to determine the propeller static thrust, and the experimental setup is depicted in Fig. 3(a). Additionally, a numerical simulation was conducted for the propeller alone configuration with a velocity of 1m/s and eight different RPM values (1000 to 8000 RPM). The propeller static thrust experiments were conducted in an outdoor environment with a measured ambient air velocity of 1 m/s. Consequently, a free stream velocity of 1 m/s was utilized in the numerical simulations to ensure the accuracy of the CFD results. The results of the streamlines are shown in Fig. 3(b), and the propeller static thrust values obtained from experiments and CFD simulations are shown in Fig. 4.

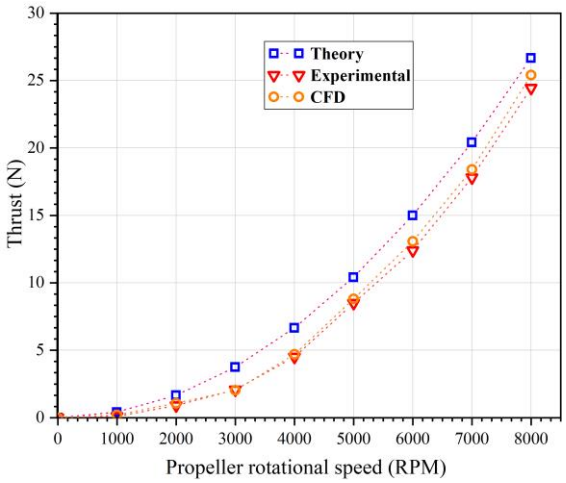

Fig. 4 Propeller static thrust results

Five different sets of tunnel tests were conducted for this study. The first set involved an investigation with no propeller, referred to as "unpowered cases." The remaining four sets tested the propeller at various rotational speeds, denoted by different advance ratios (J) of 0.45, 0.55, 0.65 and 0.75 and this is referred as “powered cases”. The propeller slipstream effects were evaluated by comparing the data from the unpowered configuration. Angles of attack (AoA) varied from -8° to +8° in increments of 4° and from +8° to +16° in increments of 1°.

All testing conditions are listed in Table 2. Prior to conducting the experiment, the three-component strain gauge internal balance underwent calibration to establish an inverse coefficient matrix for converting output voltages into forces. During wind-tunnel testing, the force matrix was derived by multiplying this inverse coefficient matrix with the output matrix. The output matrix includes values for axial force (AF), and normal forces (N1 and N2). The axial force output is utilized for generating drag, whereas the normal forces contribute to producing lift and pitching moments. The three samples of normal force, axial force, and pitching moment were recorded, and a repeatability process was employed for entire AoAs. For each angle, at least three data points were recorded and

Table 2 Test Conditions

Test Parameters	Values
Free stream velocity, V_∞ (m/s)	15
Advance ratios (J)	0.45, 0.55, 0.65 & 0.75
Propeller rotational speed (rpm)	3000,4000,5000 & 6000
Angle of attack (AoA), α (˚)	-8˚, -4˚, 0˚, 4˚, 8˚, 9˚, 10˚, 11˚, 12˚, 13˚, 14˚, 15˚ & 16˚.
Outcomes	C_L, C_D & C_M

Table 3 Uncertainty values

Parameters	Values
Velocity	± 1.173%
Advance ratio	± 1.176%
Axial force	± 0.793%
Normal force	± 0.461%

kept consistent throughout the experiments and with the support of calibration and transformation matrices, the acquired voltage signals at the balancing center were converted to forces and moments about the point of interest (on the model). Throughout the testing procedure, the stages enlisted below were followed consistently. For each test, three data sets have been obtained.

1. Wind off data: This specific run data is used to record the dead loads on the model mounted in the test section such as balancing noise and the model mounting mechanism vibrations; and
2. Wind on data: This data is obtained by setting the wind within the tunnel to the required value and by taking a sweeping test of the model, the data from the load balance is retrieved. The dry-running data from the wind must be removed from this wind on data to create data to generate aerodynamic forces and moments of the model.

To determine actual lift and drag of TMAV model, the thrust generated by the propeller was subtracted from the aerodynamic force measured in the normal and streamwise directions using the wind tunnel internal balance. The model blockage ratio within the tunnel test segment was less than 2.2%. The uncertainty associated with the experiments is shown in Table 3.

3.2 CFD Approach

This study presents wind tunnel test data alongside numerical analysis of the TMAV configuration at 15 m/s and an advance ratio of 0.45. ANSYS-Fluent software solved the Reynolds-Averaged Navier-Stokes (RANS) equations using a computational fluid dynamics (CFD) approach. To simulate the rotation of propeller blades, several methodologies are employed, including the disk-actuator model, the sliding mesh method, the Multiple Reference Frame (MRF) approach, and the dynamic mesh technique. In this research work, MRF technique is utilized for the bring a relative motion between the flow field and the propeller (Liu et al., 2011; Wang & Zhou, 2022). The MRF model employs a steady-state approximation, wherein distinct cell zones utilize different frame equations to solve the Navier-Stokes equations. The computational domain was divided into rotating and stationary zones interconnected with a non-conformal mesh. Stationary frame equations are utilized to solve for stationary zones, while rotating reference frame equations are applied to zones containing rotating components. The local reference frame changes occurring at the outer boundaries of cell zones. This allows for the seamless transfer of flow parameters from one zone to another, thereby facilitating the determination of fluxes at the interface between adjacent zones. In regions employing a rotating reference frame, velocities and their gradients are transformed from the rotating reference frame to the absolute inertial frame. Conversely, scalar magnitudes are computed locally from surrounding cells, as vector magnitudes vary with the reference frame.

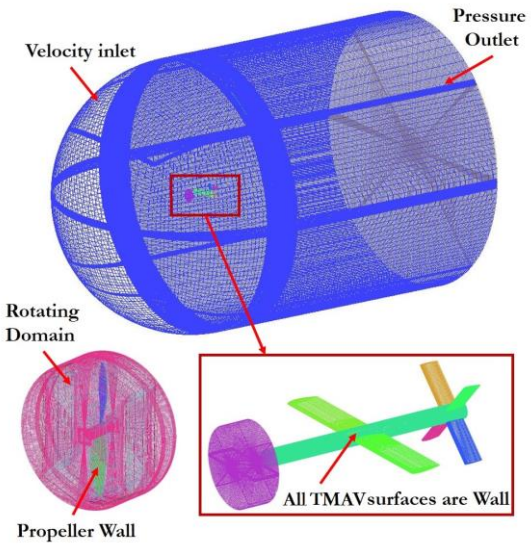

Fig. 5 computational domain and boundary conditions

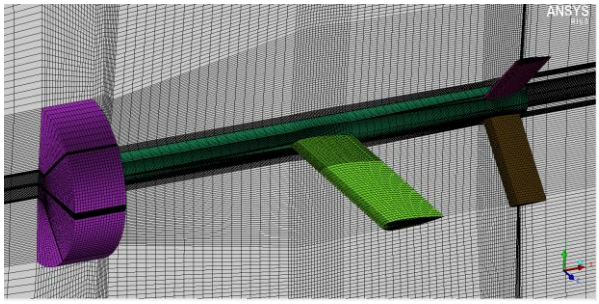

Fig. 6 Structured mesh over TMAV surfaces

In this method computational resources and time can be significantly saved, and the results can be shown with reasonable accuracy compared to unsteady approach. Inlet conditions included flow velocity, direction, turbulent intensity, and length scale, while the outlet was set as a pressure outlet. Propeller blades and model surfaces were wall conditions, and connecting faces between domains were mesh interference faces. See Fig. 5 for the computational domain and boundary conditions.

Structured meshes were generated for both the stationary and rotational domains, as depicted in Fig. 6. Inflation layers, comprising 20 cells with a first cell distance of 0.002 mm, were applied perpendicular to the TMAV surfaces and propeller blade surfaces to achieve a Y^+ value less than 1.

Due to the lack of available numerical solutions for this model configuration, a comprehensive Grid Convergence Index (GCI) investigation was conducted following the guidelines and techniques outlined by (Slater, 2000) to verify numerical calculations. The objective of this GCI study is to determine an appropriate grid resolution and

Table 4 GCI Study Results

Grid Levels(count)	*k*-ω SST model		Spalart-Allmaras model	
	C_D	GCI	C_D	GCI
Coarse mesh (4.5M)	0.3102	0.9882	0.2683	0.9479
Medium mesh (7M)	0.3139		0.2831	
Fine mesh (10M)	0.3142		0.2844	

computing resource needs, as well as to assess the performance of turbulence models for the final analysis. Three types of grids were generated for the GCI investigation, as shown in Table 4. The coefficient of drag was chosen as the functional for the GCI investigation.

In this investigation, the performance of two turbulence models, the *k*-*ω* SST turbulence model and the Spalart-Allmaras (SA) model, was evaluated. GCI_{23} represents the factor between medium and coarse grids, and GCI_{12} represents the factor between fine and medium grids, as defined by (Slater, 2000). These factors, defined in Eqs. (2) and (3), are used to compute the total GCI for the asymptotic range of convergence. This investigation was carried out for a TMAV at an AoA of 16° and J=0.45. The results of the GCI investigations are presented in Table 4. The GCI is stated as follows:

$$CGI_{12} = \frac{F_s(C_{D1} - C_{D2})}{C_{D1}(r^P - 1)} \tag{2}$$

$$CGI_{23} = \frac{F_s(C_{D2} - C_{D3})}{C_{D2}(r^P - 1)} \tag{3}$$

$$CGI = \frac{1}{r^p}\left[\frac{GCI_{23}}{GCI_{12}}\right] \tag{4}$$

In the aforementioned equations, C_{D1}, C_{D2}, and C_{D3} represent the drag coefficient values for the coarse, medium, and fine mesh cases, respectively. The factor of safety is denoted as F_S and is recommended to be 1.5 for a three-grid comparison (Slater, 2000). The grid refinement ratio, r, is defined as the ratio of the fine mesh count to the medium mesh count or the medium mesh count to the coarse mesh count. Lastly, p represents the order of accuracy.

$$p = \ln\left(\frac{C_{D3} - C_{D2}}{C_{D2} - C_{D1}}\right) / \ln(r) \tag{5}$$

The SA model is a single equation conservation model. This turbulence model is capable of accurately predicting regular flows; however, it is unable to simulate flows with small scale separations or circulation. The *k*-*ω* model resolves two supplementary conservation equations: one relates to the turbulent kinetic energy (*k*), while the other relates to the inverse time scale (*ω*). The *k*-*ω* SST model is suitable for complex three-dimensional flows with significant rotational effects, whereas the standard *k*-*ω* model is typically employed for low-Reynolds number flows (Liu et al., 2011) . Based on the GCI investigation results, both turbulent models provide nearly identical results. However, the *k*-*ω* SST turbulent model yields a value closer to 1 (GCI's asymptotic range) compared to the SA turbulent model. Therefore, the *k*-*ω* SST model was selected for the this CFD studies.

The results demonstrate that the CFD drag coefficients match the experimental data well, and the differences between medium and fine grid sizes are minimal. Considering the available computational resources and grid convergence results, the final model had approximately eight million grid elements. The pressure-based, steady-state, and coupled solver in Fluent was used with second-order spatial discretization equations.

4. RESULTS AND DISCUSSIONS

The outcomes of wind tunnel tests are presented in this section. Additionally, a few results of the experiment are compared to the results of CFD simulations, helping validate the experimental results. The aerodynamic and stability characteristics of the TMAV configuration under a flight speed of 15m/s and various propeller rotational speeds were investigated using wind tunnel studies. Furthermore, CFD simulations were conducted for the complete range of angles of attack (AoA), with a single propeller rotation speed (J=0.45) considered. The experimental and numerical simulation results are compared in this section.

4.1 Effects of Propeller Advance Ratios

4.1.1 Lift and Drag

The propeller advance ratio (J) affects the lift and drag coefficients discussed here. A Fig. 7(a) displays the coefficient of lift (C_L) for various propeller advance ratios of TMAV configurations obtained from the present studies. The first notable observation from all-powered testing is that the C_L is lower than in the unpowered tests. Additionally, the stall point occurs at an earlier AoA in the powered tests compared to the unpowered tests.

In the experimental study, the C_L is observed to decrease when comparing powered cases to unpowered cases. This reduction is evident at 11˚ AoA in powered cases, whereas in unpowered cases, the maximum C_L is observed at 14˚ AoA. The maximum C_L is reduced by 51.6% when compared to the unpowered case. In powered cases, the variation of the C_L after the stall is minimal. A more significant decrease in lift performance at higher angles (10˚ to 16˚).

When increasing the motor rotation speed, the C_L also linearly increases for all AoAs in powered tests. When the rotational speed of the propeller increases, the increase in C_L changes from 5.12% to 6.95%. This is because of the enhanced airflow over the wing and tails caused by propeller-slipstream flow. This flow created by the propeller causes areas of upwash and downwash airflow around the wing and tail. This upwash and downwash alter the local AoA of the wing and tail. The upward-going blade enhances the local AoA compared to the downward-

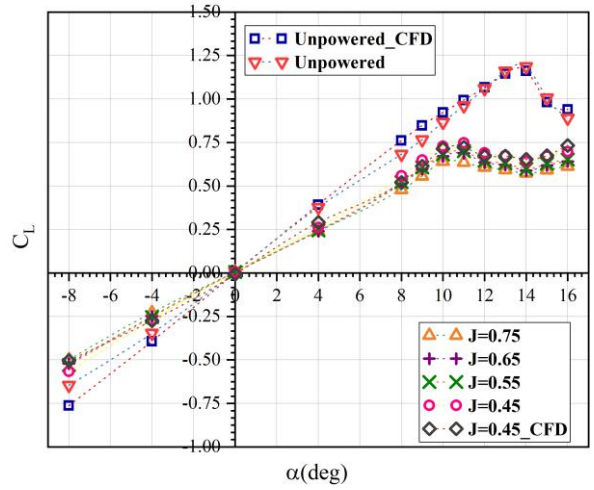

(a)

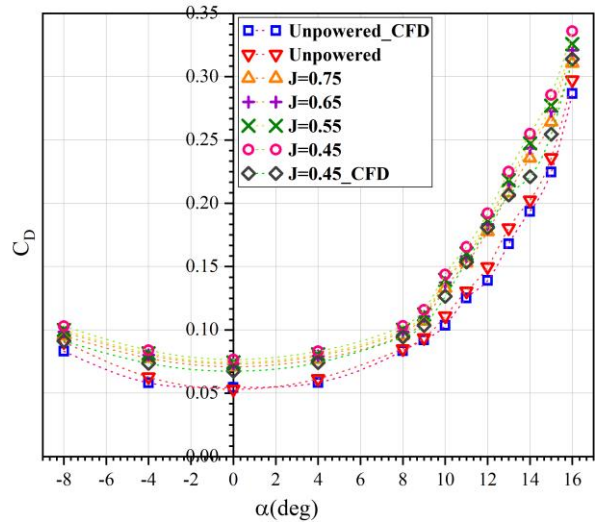

(b)

Fig. 7 Effect of propeller advance ratio on (a) lift coefficients, (b) drag coefficients

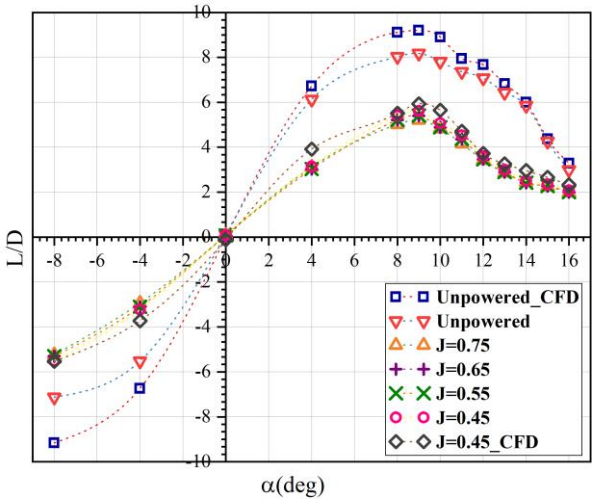

(a)

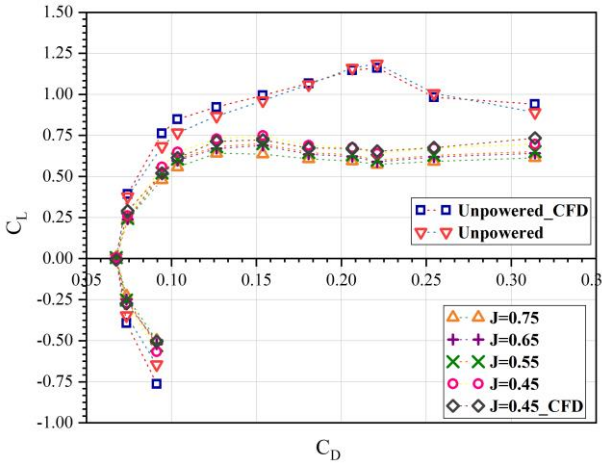

(b)

Fig. 8 Effect of propeller advance ratio on (a) lift to drag ratio (b) drag polar

going blade, resulting in pressure differences between the starboard and port wings and the four tails. This disrupts the lift generation of the wing and tails. In all powered cases, the overall lift characteristics exhibit minimal reduction in CL up to 10˚, beyond which the reduction in CL becomes more pronounced compared to unpowered cases.

In Fig. 7(b), the drag coefficient shows a gradual increase as the angle of attack increases, while the propeller rotational speeds change. The minimum drag occurs at 0˚ AoA for both powered and unpowered cases. The C_D increases by up to 44.02% in the powered case (J=0.45) compared to the unpowered case. When increasing the motor rotation speed, the C_D also linearly increases for all AoAs in powered tests. when the advance ratio reduces, the increase in C_D changes from 1.57% to 3.23%. The incremental drag does not exhibit variation similar to the C_L plot; rather, it linearly varies across all AoA due to the additive kinetic energies from both free stream and slipstream flows, consequently contributing to increased drag. Accounting for the effects of the propeller-induced slipstream results in a reduction of both the maximum lift coefficient and the lift curve slope. This leads to a slight increase in drag while simultaneously reducing the maximum lift-to-drag ratio.

4.1.2 Aerodynamic Performance

The propeller advance ratio (J) affects the lift to drag ratio discussed here. A Fig. 8(a) displays the coefficient of lift (C_L) for various propeller advance ratios of TMAV configurations. As the propeller spins, it creates a complex airflow around the TMAV, influencing aerodynamic forces. This induced flow alters the lift coefficients, reducing the efficiency of lift generation. Additionally, the increased airflow disturbances caused by the propeller result in higher drag coefficients, as the TMAV encounters greater resistance to forward motion. Consequently, the combination of decreased lift and increased drag leads to a decrease in the lift-to-drag ratios.

The maximum L/D ratio for an unpowered TMAV is 9.21, while for a powered TMAV, it is 5.61. In both powered and unpowered cases, the maximum L/D ratio occurs at 9˚ AoA. The maximum reduction in L/D ratio is 40.65% when propeller power is utilized. The section 4.2

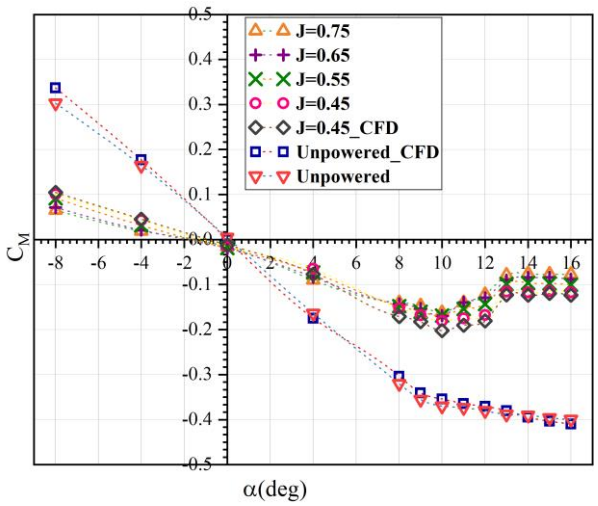

Fig. 9 Effect of propeller advance ratio on pitching moment coefficients

elucidates the flow physics governing the interaction between propeller slipstream and TMAV surfaces. This section contributes to understanding the variations in lift and drag over TMAV by examining their decrement and increment. In the stall region and at low AoAs, the percentage reduction in L/D ratio is notably high, while it decreases at higher AoAs in powered cases.

The experimental and CFD drag polar results curve for both powered and unpowered are illustrated in Fig. 8(b). From the plot, we notice that the zero lift drag coefficient (C_{D0}) for the powered TMAV is measured at 0.073, while for the unpowered TMAV, it is recorded at 0.054. Additionally, comparing experimental data with CFD simulations enhances our understanding of the aerodynamic behaviour of TMAVs and validates the accuracy of computational models. The maximum lift occurs when C_D is 0.225 for unpowered cases. However, in powered cases, C_L does not increase significantly as C_D increases.

4.1.3 Pitching Moment

A Fig. 9 shows the experimental and numerical results of pitching moment coefficient changes with variations in the angle of attack for both powered and unpowered cases. In unpowered cases, the pitching moment coefficient (C_M) remains stable across different AoAs, indicating consistent aerodynamic behaviour. However, in powered cases, the behaviour of C_M varies with changes in AoA. Up to an AoA of 10˚ AoA, the C_M remains stable, suggesting that the TMAV maintains its pitching stability within this range. Beyond 10˚ to 13˚ AoA, the powered cases exhibit unstable behaviour in C_M.

This instability indicates that the TMAV experiences a tendency to pitch uncontrollably, potentially leading to difficulties in maintaining its desired orientation. This instability arises from the combined effects of the propeller slipstream flow and the angle of attack of the TMAV, which collectively position the center of pressure (CP) ahead of the center of gravity (CG). Consequently, the TMAV is subjected to unstable pitching moments. From 14˚ to 16˚ AoAs, the C_M shows neutral stability,

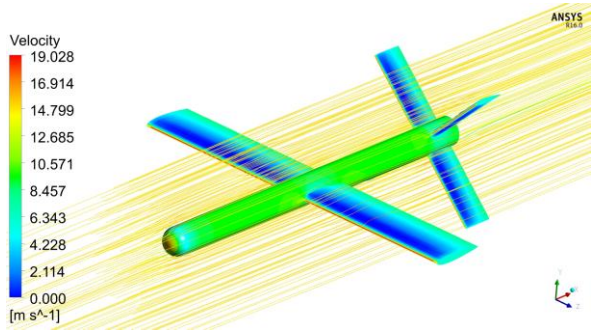

(a) J=0, α = 0˚

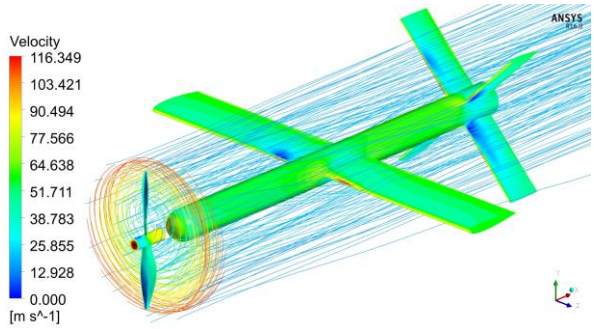

(b) J=0.45, α = 0˚

Fig. 10 Stream lines over the TMAV

(a) unpowered (b) powered

meaning there is no tendency for the TMAV to pitch either upward or downward. This suggests that the TMAV is in a balanced state in terms of pitching moment at these AoAs. The addition of the motor/propeller to the TMAV results in a significant difference in C_M compared to unpowered cases. This difference highlights the influence of propulsion on the aerodynamic characteristics of the TMAV, particularly in terms of its pitching behavior.

4.2 Effect of Propeller Slipstream on TMAV Surfaces

In this section, explain the details of propeller slipstream effects on each component of the TMAV, particularly pressure distribution over the components. A Fig. 10 shows the pressure variation of each TMAV component with and without power, as well as the streamlines over the TMAV. The primary focus is on the wing and X-tail, with an in-depth investigation of the body also presented.

4.2.1 Planar Wings

While propeller rotation affects the entire flow field surrounding the TMAV, its impact on each component varies. The wing is the primary component responsible for generating lift. Therefore, determining whether the slipstream has a noticeable impact on the wing is particularly significant.

The surface pressure contours for both wings (α = 0˚) are shown for powered and unpowered conditions in Fig. 10. A Fig. 11 displays the pressure contour for the port wing alone. The starboard wing likely has a similar, but mirrored, contour. The quantities differ for both wings in the powered case.

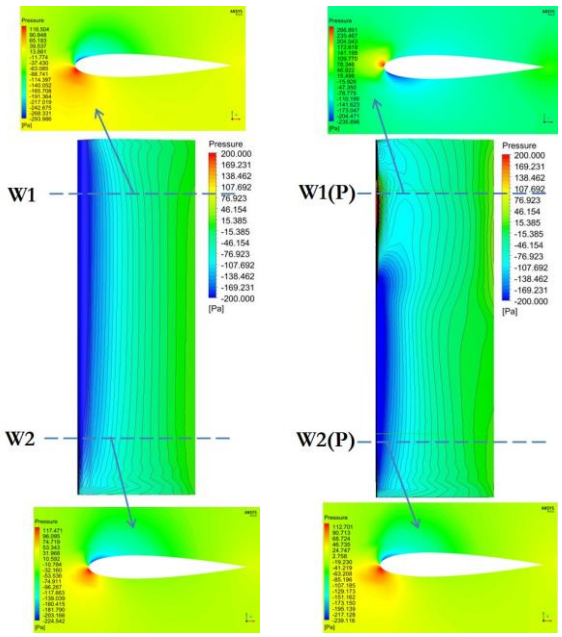

(a) J=0, α = 8˚ (b) J=0.45, α = 8˚

Fig. 11 Wing pressure contours

(a) unpowered (b) powered

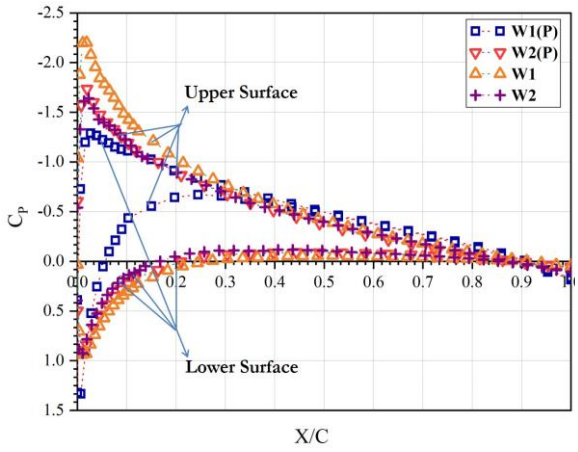

Fig. 12 Pressure coefficients distribution over wing section (α = 8˚)

For the unpowered case, both wings have similar contours for each AoAs. The upper (near wing root side) wing pressure contours exhibit notable variations between the configurations with and without the propeller, as depicted in Fig. 11. The propeller swirl flow (upwash) generates a high-pressure region on the upper surface of the root side and a low-pressure region on the lower surface of root side, as shown in Fig. 11 and denoted at location W1(P). Changes on the tip side are minimal, denoted as W2(P), and are similar to the unpowered wing contour denoted as W1 and W2.

In order to conduct a more detailed study, the pressure coefficients of wing sections are obtained at various places along the semi-wingspan, namely denoted as W1(P), W2(P), W1, and W2. These positions are illustrated in Fig. 12. The C_P curve (W1(P)) indicates that on the upper surface, the curve initially starts at a positive C_P value but

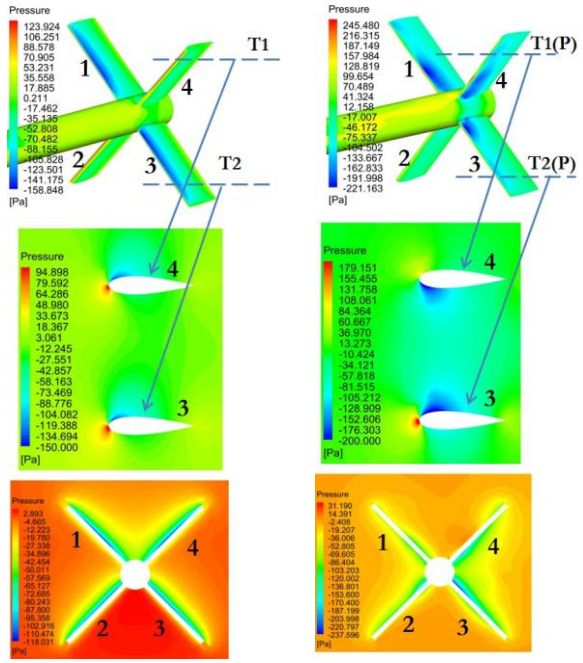

(a) J=0, α = 8˚ (b) J=0.45, α = 8˚

Fig. 13 X-tails pressure contours (a) unpowered (b) powered

transitions to a negative C_P value after a certain distance, attributed to the propeller-induced upwash flow.

This results in lift loss on the port wing and an increase in lift on the star board side due to propeller upwash flow increases flow local AoA. The C_P curve on the lower surface of the port wing is consistently negative compared to unpowered lower surface curves, indicating low C_P values. The C_P curve (W2(P)) almost matches the W2 curve, suggesting that the propeller slipstream on the wingtip side has negligible effects.

4.2.2 X-Tail

The X-tail is crucial for maintaining longitudinal stability in an TMAV. However, its placement in the propeller slipstream can disrupt the flow field passing through the X-tail, leading to significant changes. The influence of the propeller's swirl flow field on the X-tail force would be completely different from that of unpowered cases. The pressure distribution on the X-tail is symmetrical when there is no propeller flow, but becomes disorganized when a propeller flow is present. The surface pressure contours for tails (α = 0˚) are shown for powered and unpowered conditions in Fig. 10. A Fig. 13 presents the pressure section contour for tails 3 and 4. Tails 1 and 2 likely exhibit a similar but mirrored contour, with quantities differing in the powered case. In the unpowered case, all tails display similar contours across all AoAs.

In Fig. 13(a), pressure variations are similar for all tails in unpowered cases, but differ in powered cases. A Fig. 13(b) shows that the upper surface pressure distribution of tail 4 is higher compared to unpowered cases, while the lower surface has lower pressure distribution. This is due to propeller upwash flow directly hitting the upper surface

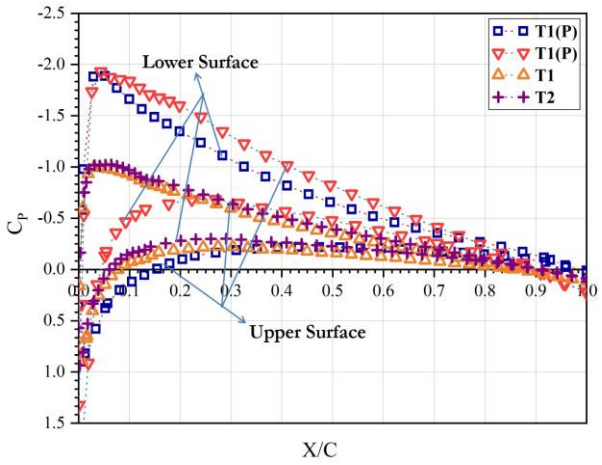

Fig. 14 Pressure coefficients distribution over tail section (α = 8˚)

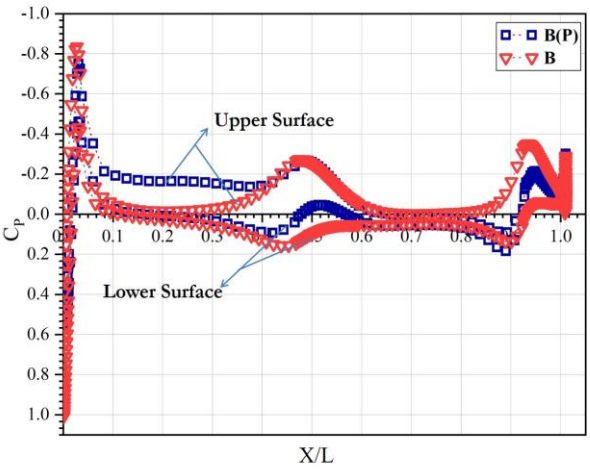

Fig. 16 Pressure coefficients distribution over body (α = 8˚)

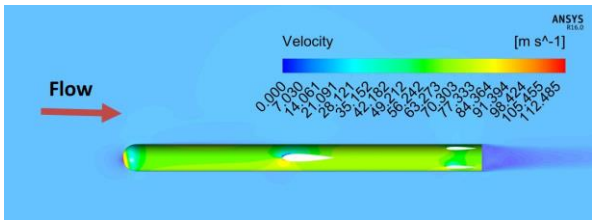

(a) J=0, α = 8˚

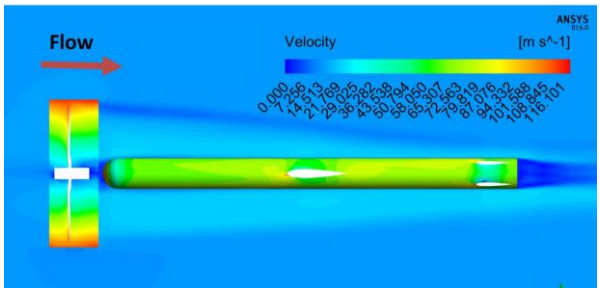

(b) J=0.45, α = 8˚

Fig. 15 Body pressure contours (a) unpowered (b) powered

of tail 4 and downwash flow hitting the lower surface of tail 2. It can be observed in Fig. 13(b), the X-tail section cut contour.

The pressure coefficients of tail 4 and 3 sections are obtained at various places along the tail span, namely denoted as T1(P), T2(P), T1, and T2. These positions are illustrated in Fig. 14. In the unpowered cases, the C_P distributions of tails 3 and 4 are similar, but in the powered cases, they are quite different. For tail 3, both the upper and lower surface C_P plots are located in the negative region. However, for tail 4, a certain distance from the leading-edge portion on the upper surface, the C_P is positive, while its lower surface C_P is entirely negative, causing the negative lift provided by tail 4.

4.2.3 Circular Body

The body gives a considerable contribution to the forces and moments of the TMAV. A Fig. 15 displays the pressure contour for the body for both unpowered and powered cases. It can be observed that in the unpowered case, flow changes are slightly symmetrical about the horizontal axis, whereas in powered cases, slipstream flow alters over the entire body.

The C_P plot over the body for unpowered (B) and powered (B(P)) cases is shown in Fig. 16. The unpowered cases upper and lower surface plots are cover area is slightly greater than powered cases.

4.3 Break Down of Parameters

The overall forces and moments acting on the TMAV are discussed in section 4.1. In the discussed section, there is a breakdown of the aerodynamic parameters of each component. These results are derived from numerical analysis at α = 8˚ for both unpowered and powered cases. The propeller slipstream effect on C_L is found in the body, wing, and tails. A Fig. 17 (a) shows the breakdown of the C_L on the TMAV components. The propeller upwash flow reduces the C_L for the body, port wing, tail 1, 2 and 4, while the downwash flow slightly increases the C_L for the starboard wing, and tail 3. The overall C_L for powered cases is less compared to unpowered cases.

A Fig. 17(b) shows the breakdown of the C_D on the TMAV components. All values of C_D are increasing except for the port wing and tail 4. A tail 4 provides negative drag due to the propeller upwash flow striking the tail 4 leading edge portion, opposing the motion of the TMAV.

The overall C_M reduces when the propeller is powered, and the C_M of each component is listed in Fig. 17(c). The body does not contribute to the C_M in the unpowered case; however, in the powered case, it exhibits a negative moment. In the unpowered case, both wings generate negative moments, but in powered cases, the port wing produces a positive moment due to propeller upwash flow, while the starboard wing generates a negative moment due to propeller downwash flow. All tails provide positive moments in unpowered cases, but in powered cases, only tail 2 and 3 exhibit positive moments. The other tails both

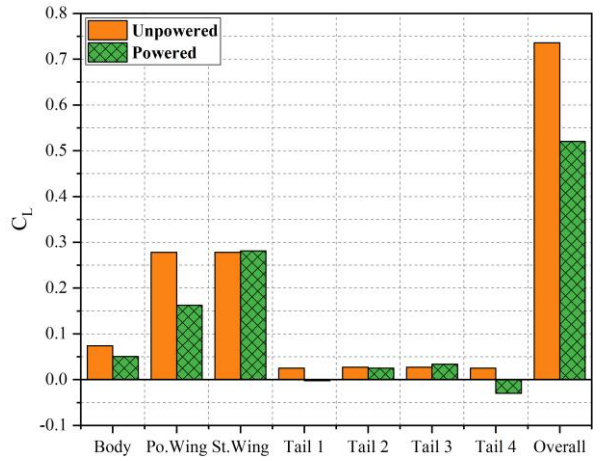

(a) C_L

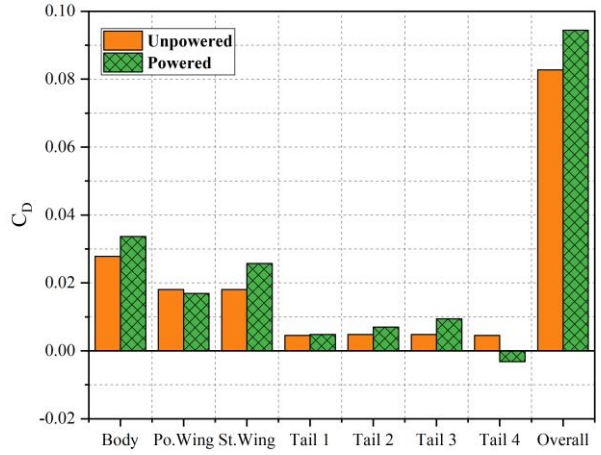

(b) C_D

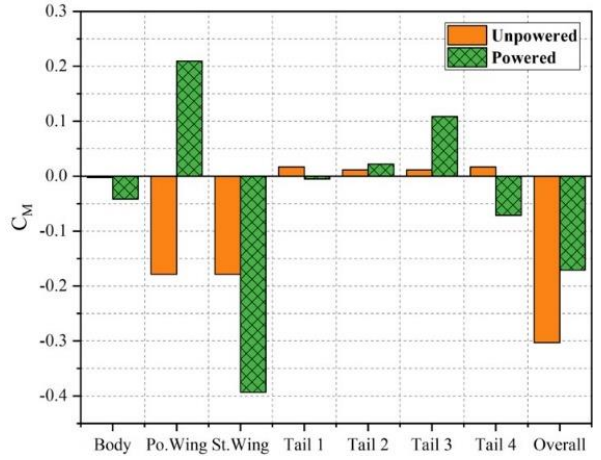

(c) C_M

Fig. 17 Aerodynamic parameters variation on TMAV components at J=0.45 and α = 8˚.

exhibit negative moments due to disturbances from propeller upwash flow.

5. CONCLUSION

The present study investigates the effects of propeller slipstream on transition micro air vehicles through wind tunnel experiments and numerical simulations. The aerodynamic forces and moments of both powered (J=0.45, 0.55, 0.65 & 0.75) and unpowered cases are measured in the experiments. Numerical simulations were conducted to analyse the slipstream effect using the MRF method for both unpowered and powered (J=0.45) cases.

1. The slipstream effects significantly influenced the total lift of the vehicle. In powered scenarios, the total lift of the TMAV was reduced compared to the unpowered scenario. In the unpowered case, the maximum lift coefficient occurs at 14° AoA, while in the powered case, it occurs at 11° AoA. The maximum CL is reduced by 51.6% compared to the unpowered case.
2. The drag coefficients are increased by slipstream flows and it increases by 44.02% in the powered cases. When the advance ratio reduces from 0.75 to 0.45, the maximum C_L increases from 5.12% to 6.95%, and the minimum C_D increases from 1.57% to 3.23%.
3. The propeller slipstream flows result in a reduction of the L/D ratios. The maximum L/D ratio occurs at 9˚ AoA for both powered and unpowered conditions. In the powered cases, the maximum L/D ratio is reduced by 40.65%.
4. In powered scenarios, the slipstream flows cause the centre of pressure to shift ahead of the CG at angles of attack exceeding 10˚. Between 10˚ and 13˚ AoA, it shows unstable behaviour, and beyond 13˚ AoA, the pitching moment remains almost constant.
5. The slipstream upwash and downwash flows alter the aerodynamic characteristics of wings and tails. Specifically, the root side of the wings is affected by slipstream flows, causing the upper surface of the port wing to experience higher pressure and the lower surface to experience lower pressure. Conversely, the starboard wing exhibits the opposite effect. As a result, the lift and drag coefficient of the port wing is lower compared to the starboard wing.
6. All four tails have been influenced by slipstream swirl flows. Tail 1 and tail 4 exhibit significant surface effects, where tail 1 experiences reduced lift, and tail 4 generates negative lift.

Overall, the propeller slipstream decreases aerodynamic performance and stability parameters. The slipstream flows reduce the lift coefficients, leading to earlier stall occurrences, as well as producing additional drag and reduced pitching moments

ACKNOWLEDGEMENTS

The contribution by the late Dr. S. Pannerselvam is gratefully acknowledged by the authors and would like to thank Dr. D.R. Biju Ben Rose, Dr. Swagata Paul, and Mr. K. Pounraj for their contributions during wind tunnel testings.

CONFLICT OF INTEREST

The authors have no conflict of interest to disclose this research work.

AUTHORS CONTRIBUTION

A. Vinoth Raj: Writing – original draft, Investigation, Conceptualization, Methodology, Formal

analysis, Data curation. **C. Senthil Kumar:** Conceptualization, Methodology, Resources, Writing – review & editing, Supervision.

REFERENCES

Ahn, J., & Lee, D. (2013). *Aerodynamic characteristics of a micro air vehicle and the influence of propeller location.* 31st AIAA Applied Aerodynamics Conference, 1–9. https://doi.org/10.2514/6.2013-2655

Aminaei, H., Dehghan Manshadi, M., & Mostofizadeh, A. R. (2019). Experimental investigation of propeller slipstream effects on the wing aerodynamics and boundary layer treatment at low Reynolds number. *Proceedings of the Institution of Mechanical Engineers, Part G: Journal of Aerospace Engineering*, *233*(8), 3033–3041. https://doi.org/10.1177/0954410018793703

Ananda, G. K., Deters, R. W., & Selig, M. S. (2013). *Propeller induced flow effects on wings at low Reynolds numbers.* 31st AIAA Applied Aerodynamics Conference, 1–20. https://doi.org/10.2514/6.2013-3193

Ananda, G. K., Deters, R. W., & Selig, M. S. (2014, June). *Propeller-induced flow effects on wings of varying aspect ratio at low reynolds numbers.* 32nd AIAA Applied Aerodynamics Conference, 1–20. https://doi.org/10.2514/6.2014-2152

Ananda, G. K., Selig, M. S., & Deters, R. W. (2018). Experiments of propeller-induced flow effects on a low-Reynolds-number wing. *AIAA Journal*, *56*(8), 3279–3294. https://doi.org/10.2514/1.J056667

Arivoli, D., Dodamani, R., Antony, R., Suraj, C. S., Ramesh, G., & Ahmed, S. (2011, June, 1–10). *Experimental Studies on a Propelled Micro Air Vehicle.* 29th AIAA Applied Aerodynamics Conference 2011. https://doi.org/10.2514/6.2011-3656

Balaji, G., Pillai, S. N., & Senthil Kumar, C. (2017). Wind Tunnel Investigation of Downstream Wake Characteristics on Circular Cylinder with Various Taper Ratios. *Journal of Applied Fluid Mechanics*, 10 (Special Issue), 69–77. https://doi.org/10.36884/jafm.10.SI.28272

Bansal, U., Sinduraa, B. V., Panneerselvam, S., & Santhakumar, S. (2011). Design and Development of a Transitional Micro Air Vehicle. *Symposium on Applied Aerodynamics and Design of Aerospace Vehicles* (SAROD November - 2011).

Cao, M., Liu, K., Wang, C., Wei, J., & Qin, Z. (2023). Research on the distributed propeller slipstream effect of UAV wing based on the actuator disk method. *Drones*, *7*(9). https://doi.org/10.3390/drones7090566

Catalano, F. M. (2004). On the effects of an installed propeller slipstream on wing aerodynamic characteristics. *Acta Polytechnica*, *44*(3). https://doi.org/10.14311/562

Chen, G., Chen, B., Li, P., Bai, P., & Ji, C. (2015). Numerical simulation study on propeller slipstream interference of high altitude long endurance unmanned air vehicle. *Procedia Engineering*, *99*, 361–367. https://doi.org/10.1016/j.proeng.2014.12.548

Chen, Z., & Yang, F. (2022). Propeller slipstream effect on aerodynamic characteristics of micro air vehicle at low reynolds number. *Applied Sciences (Switzerland)*, *12*(8). https://doi.org/10.3390/app12084092

Chinwicharnam, K., & Thipyopas, C. (2016). Comparison of wing-propeller interaction in tractor and pusher configuration. *International Journal of Micro Air Vehicles*, *8*(1), 3–20. https://doi.org/10.1177/1756829316638206

Cho, J. H. (2014). Experimental and numerical investigation of the power-on effect for a propeller-driven UAV. *Aerospace Science and Technology*, *36*, 55–63. https://doi.org/10.1016/j.ast.2014.04.001

Durai, A. (2014). Experimental investigation of lift and drag characteristics of a typical MAV under propeller induced flow. *International Journal of Micro Air Vehicles*, *6*(1), 63–72. https://doi.org/10.1260/1756-8293.6.1.63

Figat, M., & Piątkowska, P. (2020). Numerical investigation of mutual interaction between a pusher propeller and a fuselage. *Proceedings of the Institution of Mechanical Engineers, Part G: Journal of Aerospace Engineering*, *0*(0), 1–14. https://doi.org/10.1177/0954410020932796

Furusawa, Y., Kitamura, K., Ikami, T., Nagai, H., & Oyama, A. (2024). Numerical study on aerodynamic characteristics of wing within propeller slipstream at low-reynolds-number. *Transactions of the Japan Society for Aeronautical and Space Sciences*, *67*(1), 12–22. https://doi.org/10.2322/tjsass.67.12

Gabriel, S. (2013). Propeller Static & Dynamic Thrust Calculation. https://www.electricrcaircraftguy.com/2013/09/propeller-static-dynamic-thrust-equation.html.

Hassanalian, M., Khaki, H., & Khosravi, M. (2015). A new method for design of fixed wing micro air vehicle. *Proceedings of the Institution of Mechanical Engineers, Part G: Journal of Aerospace Engineering*, *229*(5), 837–850. https://doi.org/10.1177/0954410014540621

Jana, S., Kandath, H., Shewale, M., & Bhat, M. S. (2020). Effect of propeller-induced flow on the performance of biplane micro air vehicle dynamics. *Proceedings of the Institution of Mechanical Engineers, Part G: Journal of Aerospace Engineering*, *234*(3), 716–728. https://doi.org/10.1177/0954410019883097

Khoshnevis, A. B., Barzenoni, V., & Mamouri, A. R. (2016). Experimental study of parameters and high - order values of velocity in the behind wake of a vehicle model, *Automotive Science and Engineering*, *6*(4), 2291-2300. https://www.iust.ac.ir/ijae/article-1-

386-en.html.

Liu, Z., Albertani, R., Moschetta, J. M., Xu, M., & Thipyopas, C. (2011). Experimental and computational evaluation of small microcoaxial rotor in hover. *Journal of Aircraft*, *48*(1), 220–229. https://doi.org/10.2514/1.C031068

Meng, X., Xu, Z., Chang, M., & Bai, J. (2023). Performance analysis and flow mechanism of channel wing considering propeller slipstream. *Chinese Journal of Aeronautics*, *36*(11), 165–184. https://doi.org/10.1016/j.cja.2023.06.022

Null, W., & Shkarayev, S. (2005). Effect of camber on the aerodynamics of adaptive-wing micro air vehicles. *Journal of Aircraft*, *42*(6), 1537–1542. https://doi.org/10.2514/1.12401

Rostami, M., & Farajollahi, A. H. (2021). Aerodynamic performance of mutual interaction tandem propellers with ducted UAV. *Aerospace Science and Technology*, *108*, 106399. https://doi.org/10.1016/j.ast.2020.106399

Sadraey, M. (2010). Unmanned Aircraft Design: A Review of Fundamentals. In Text book: Morgan & claypool Publishers (pp. 4–5). https://doi.org/10.2200/S00789ED1V01Y201707MEC004

Shams, T. A., Shah, S. I. A., Shahzad, A., Javed, A., & Mehmod, K. (2020). Experimental investigation of propeller induced flow on flying wing micro aerial vehicle for improved 6DOF modeling. *IEEE Access*, *8*, 179626–179647. https://doi.org/10.1109/ACCESS.2020.3026005

Sharma, P., & Atkins, E. (2019). Experimental investigation of tractor and pusher hexacopter performance. *Journal of Aircraft*, *56*(5), 1920–1934. https://doi.org/10.2514/1.C035319

Slater, J. W., Dudek, J. C., & Tatum, K. E. (2000). The NPARC alliance verification and validation archive. American Society of Mechanical Engineers, Fluids Engineering Division (Publication) FED, 251(April), 1005–1012. https://ntrs.nasa.gov/citations/20000054672

Sudhakar, S., Kumar, C., Arivoli, D., Dodamani, R., & Venkatakrishnan, L. (2013, January 1–10). *Experimental studies of propeller induced flow over a typical micro air vehicle.* 51st AIAA Aerospace Sciences Meeting Including the New Horizons Forum and Aerospace Exposition 2013. https://doi.org/10.2514/6.2013-60

Suresh, V., Premkumar, P. S., & Senthilkumar, C. (2019). Drag reduction of non-circular cylinder at subcritical reynolds numbers. *Journal of Applied Fluid Mechanics*, *12*(1), 187–194. https://doi.org/10.29252/jafm.75.253.28686

Teixeira, P. C., & Cesnik, C. E. S. (2019). Propeller effects on the response of high-altitude long-endurance aircraft. *AIAA Journal*, *57*(10), 4328–4342. https://doi.org/10.2514/1.J057575

Wang, K., & Zhou, Z. (2022). An investigation on the aerodynamic performance of a hand-launched solar-powered UAV in flying wing configuration. *Aerospace Science and Technology*, *129*, 107804. https://doi.org/10.1016/j.ast.2022.107804

Zhang, X., Zhang, W., Li, W., Zhang, X., & Lei, T. (2023). Experimental research on aero-propulsion coupling characteristics of a distributed electric propulsion aircraft. *Chinese Journal of Aeronautics*, *36*(2), 201–212. https://doi.org/10.1016/j.cja.2022.07.024

Zhao, S., Li, J., Jiang, Y., Qian, R., & Xu, R. (2022). Investigation of propeller slipstream effects on lateral and directional static stability of transport aircraft. *Engineering Applications of Computational Fluid Mechanics*, *16*(1), 551–569. https://doi.org/10.1080/19942060.2021.1997824